PAPER

PN junction and band to band tunneling in carbon nanotube transistors at room temperature

To cite this article: Gilad Zeevi *et al* 2021 *Nanotechnology* **32** 335202

IOP Publishing Nanotechnology
Nanotechnology 32 (2021) 335202 (8pp) https://doi.org/10.1088/1361-6528/abfd56

PN junction and band to band tunneling in carbon nanotube transistors at room temperature

Gilad Zeevi, Alexey Razin and Yuval E Yaish*

Andrew and Erna Viterbi Faculty of Electrical Engineering, Technion, Haifa, Israel

E-mail: giladz@campus.technion.ac.il and yuvaly@technion.ac.il

Received 25 January 2021, revised 19 April 2021
Accepted for publication 29 April 2021
Published 24 May 2021

Abstract

We demonstrate band to band tunneling (BTBT) in a carbon nanotube (CNT) field effect transistor. We employ local electrostatic doping assisted by charged traps within the oxide to produce an intramolecular PN junction along the CNT. These characteristics apply for both metallic (m-CNTs) and semiconducting (SC-CNTs) CNTs. For m-CNTs we present a hysteretic transfer characteristic which originates from local electrostatic doping in the middle segment of the CNT. This controlled doping is reversible and results in formation and destruction of a PN junction along the CNT channel. For SC-CNTs we observe BTBT, and analysis based on the WKB approximation reveals a very narrow depletion region and high transmission probability at the optimal energy bands overlap. These results may assist in developing a non-volatile one-dimensional PN junction memory cell and designing a tunneling based field effect transistor.

Supplementary material for this article is available online

Keywords: intramolecular PN junction, carbon nanotube, low dimension, band-to-band tunneling, charge trapped

(Some figures may appear in colour only in the online journal)

Introduction

Low dimensional conductive materials have attracted large interest and produced extensive research in the last two decades as potential building blocks for integration in conventional CMOS technology. Carbon nanotube (CNT) is a versatile 1D carbon allotrope, which demonstrates excellent electronic and mechanical properties [1], and has been considered as an attractive candidate in future electrical circuits [2–5]. CNTs are generally divided into two principal groups, metallic (m-CNT) and semiconducting (SC-CNT). The former group includes CNTs with negligible band-gap, typically of the order of room temperature thermal energy (k_BT), which presents transfer characteristics very similar to graphene [6]. The latter group consists of nanotubes with a more sizable band-gap, which typically shows electrical conductivity of a single charge carrier (either hole or electron) [7, 8]. Junction between hole dominant and electron dominant segments forms a PN junction which is a basic building block in many electronic devices, such as rectifying diodes, bipolar transistors, solar cells, and light emitting diodes. And a 1D PN junction, embedded in a CNT, is a key ingredient in the scaling of such devices.

Intramolecular junctions in single-wall carbon nanotubes (SWCNTs) have been demonstrated [9–12] and further developed towards useful electronic devices [13, 14]. The common approaches in realization of PN junctions along CNTs include chemical doping [9, 15–19], or active electrostatic doping [10, 11, 13, 14, 20]. The first method is commonly non-reversible and may reduce the CNT's electrical mobility, where the second one requires a constant power supply to maintain the PN junction. In this study, we present an alternative approach for the electrochemical doping of a SWCNT. We use a double gate structure in a quasi CNT-based field effect transistor (CNTFET) to trap charges in the gate-stack and modify the device characteristics. The

* Author to whom any correspondence should be addressed.

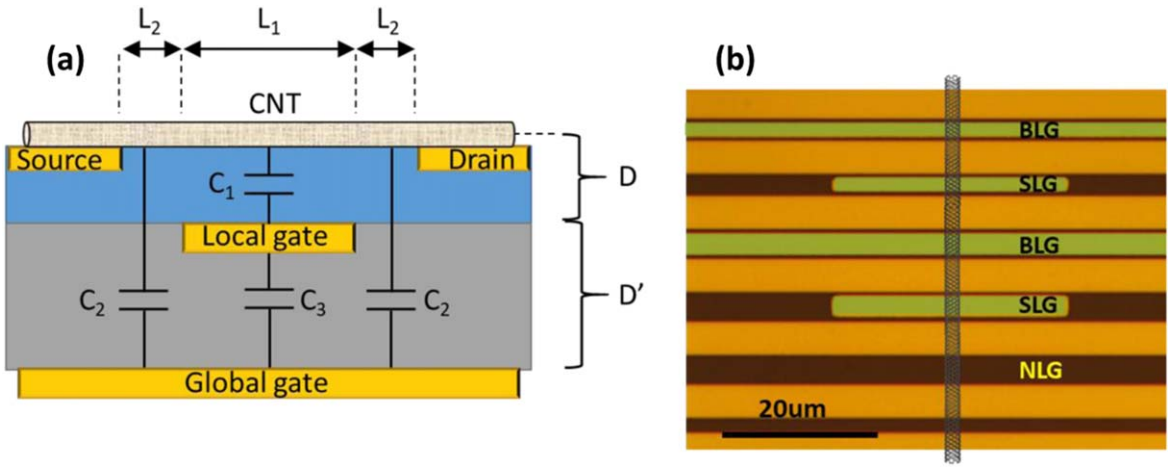

Figure 1. Device description. (a) A schematic of the device cross-section. A local gate is patterned on top of a P++ doped silicon (global gate) capped by 285 nm SiO_2 (gray). HfO_2 covers the local gate (ALD ~6 nm, blue), with electrodes (source and drain) patterned on top of the HfO_2. A CVD-grown CNT is transferred on top of the electrodes. C_1, C_2 and C_3 present the capacitances between the local gate and the CNT's L_1 segment, the global gate and the CNT's L_2 segment, and between the global and local gates, respectively. (b) Top view (optical image) of a group of devices, all sharing the same CNT. Local gates are marked in green (some are small floating gates—SLG, and others are patterned with pads—BLG, NLG is a CNTFET with no local gate) while source/drain electrodes are depicted in orange (false colors). The vertical line presents the CNT which lays on top of the electrodes.

gate-stack consists of a local gate and a thin high-k dielectric (HfO_2) with trapped charges located only few nm away from the CNT. The gate-stack can be charged/discharged by applying gate-pulses with the appropriate voltage. This approach differs from the traditional electrostatic doping, as it does not require a constant operation of an external voltage source to the local gate. This may reduce static power consumption without losing the flexibility of 'turning on/off' the PN junction along the CNT, as well as keeping the doping control of the CNT-segment. In this study we present PN junctions in both SC-CNTs and m-CNTs and analyze their performance.

Experimental details

We use a conventional electron-beam lithography and atomic layer deposition (ALD) to fabricate our devices. We begin with a P++ silicon substrate covered by a thick SiO_2 (285 nm) layer. The local gate consists of a patterned Cr/Pt structure (5/20 nm thickness, respectively) on top of the SiO_2. Then, a thin (6 nm) HfO_2 layer is deposited in ALD, forming the local gate dielectric (LGD). We open a contact to the local gate pads using reactive ion etching (RIE). Electrodes are patterned on top of the HfO_2 (Cr/Pt/Au—5/10/10 nm respectively), and finally a carbon nanotube is transferred on top of the electrodes. Figure 1(a) presents a schematic of our device, along with a capacitance model. The local gate width is shorter than the channel length, which leaves ~0.5 μm gap (marked as L_2) between the overlapped segment (marked as L_1) and the source/drain (S/D) electrodes. The heavily doped silicon serves as a global gate (V_{gg}). We divide out devices by their local gate type (figure 1(b)). One type comprises a 30 μm strip of metal floating between the CNT and the global gate at the SiO_2-HfO_2 interface (SLG). The second type of local gates resembles the first one but additionally has its own pad, which allows for a direct electrical connection with the external environment (BLG). Some devices include no local gate at all (NLG). The devices channel lengths range between 3 and 4 μm, and a single CNT is shared by a set of the different device types (figure 1(b)).

For the electrical characterization we employ two measurement protocols. (a) DC measurements (DCM) in which we sweep the gate voltage (up to $\pm$5 V) while measuring the CNT current (I_{ds}). (b) Pulse measurements (PLM), in which we apply short pulses to the local gate and subsequently sweep the V_{gg} (small sweep-range) to inspect the transfer characteristics of the device. The pulse amplitudes increase from 1 to 3 V (or -1 to -3 V) between each narrow-range V_{gg} sweep measurement.

The presence of the local gate (as presented in figure 1(a)) may shift the Fermi energy (E_F) of the L_1 segment when nonzero gate voltages are applied. By introducing strong electric fields between the local gate and the CNT (over 1 MV cm^{-1}), charge is injected from the CNT into the HfO_2 dielectric layer. This charge is trapped in the LGD and effectively shifts the Fermi energy of the CNT-segment which resides directly above it. When left floating, our devices geometry allows the local gate to act as an electrostatic lever to the voltage applied by the global gate. This allows us to maintain high electric fields between the floating local gate and the CNT, without the hazard of short current events or dielectric breakdown. Depending on the polarity of the applied V_{gg}, the LGD may be charged with negative or positive charges. The LGD charge electrostatically dopes the middle segment of the CNT (L_1), while leaving the side segments (L_2) almost unaffected, resulting in inhomogeneous doping along the CNT. By carefully choosing the right polarities of each segment one can realize a PN junctions along the CNT.

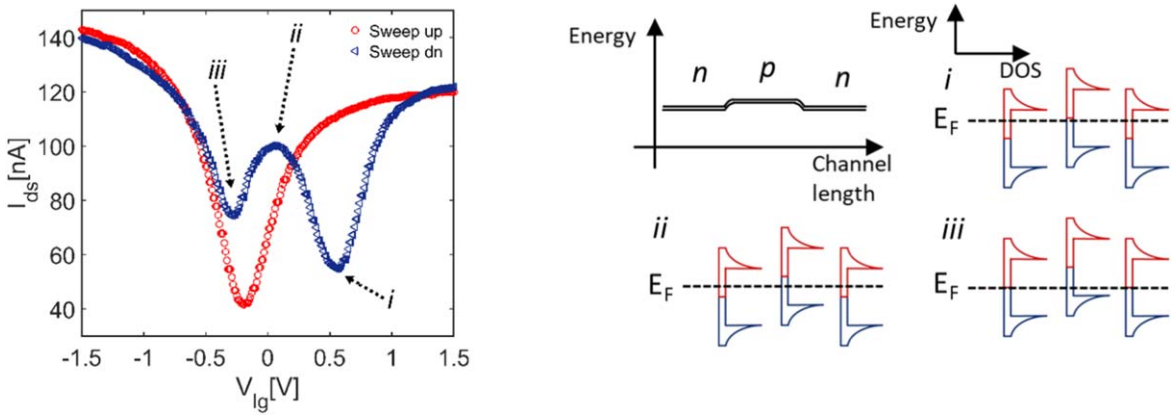

Figure 2. n−p−n quasi CNTFET. (a) Transfer characteristics with Vds = 10 mV. After V_{lg} is swept to positive 2 V, the LGD above the local gate is negatively charged, and the middle segment of the CNT is positively doped. The doping variation between the CNT's segments cause a peculiar, double minima points in the 'Sweep dn' curve (blue triangles). After V_{lg} is swept to negative −2 V, the LGD is discharged, and the middle section of the CNT is restored to its original doping-state. As a result, the 'sweep up' curve (red circles) retains a more conventional transfer characteristics form. (b) Energy band diagram along the CNT, Fermi energy, and density of state (DOS) for the different segments along a small band-gap CNT, corresponding to the points marked by arrows in 'a'.

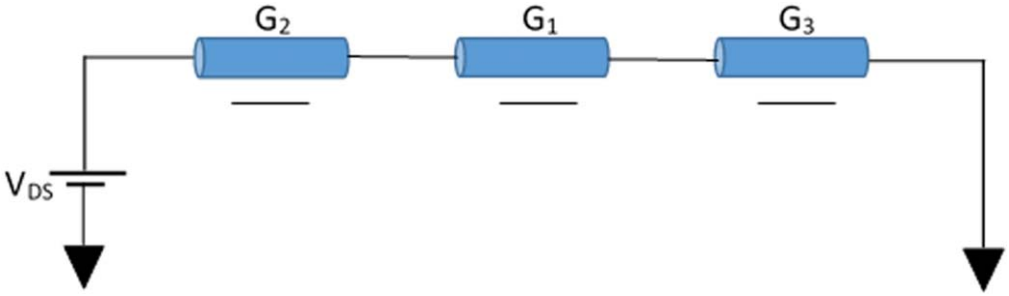

Figure 3. Equivalent electrical circuit. G_1, G_2 and G_3 represent the conductance of the different parts of our device. G_2 and G_3 include the contact resistance between the CNT and the S/D electrode. All conductances are modulated by an electric field applied by gate voltage.

Results and discussion

The signature of a PN junction along a m-CNT is presented in figure 2(a), where the local gate voltage (V_{lg}) is swept in the range of ±2 V as we measure the Ids current. At large positive V_{lg}, electrons are pulled from the CNT into the LGD. This local (negative) charge is trapped in the LGD and induces p-doping in the middle segment of the CNT. When the V_{lg} is swept down (blue marks), we see an Ids minimum at $V_{lg} \approx$ 0.6 V, (see figure 2(a), point i). As the V_{lg} is swept further down we encounter an Ids maximum point at $V_{lg} \approx 0$ V, and another minimum at $V_{lg} \approx -0.3$ V (figure 2(a), points ii and iii, respectively). At large negative V_{lg}, the charge stored in the LGD returns to the CNT and the CNT's middle segment recovers back to its original doping-state. A typical small band-gap CNT transfer characteristic appears as the V_{lg} is swept back from negative to positive voltage (red circles). Figure 2(b) presents an illustration of the EF position and the CNT's density of states (DOS) along the CNT's various segments, for the points i, ii, iii displayed in figure 2(a). At point i, EF is positioned at the Dirac point of the middle CNT-segment, while the left and right segments are n-type. At point ii, we have an intramolecular NP and PN junctions along the CNT, as EF is positioned at electron dominated left and right segments and a hole dominated middle CNT-segment. One of the PN junction is positively biased, while the other is negatively biased where band to band tunneling (BTBT) dominates the charge conduction (the transmission probability is very high due to small band-gap and relatively high doping in both sides of the PN junction, see for instance Knoch *et al* [21]). At point iii, EF is positioned at the Dirac point of the left and right segments in contrast to the hole dominated middle segment of the CNT.

We developed a conduction model to analyze the measured transfer characteristics. The CNT incorporated in our device has a small band-gap ($E_{g,CNT}$−k_BT), and therefore we assume that the tunneling probability through the reverse-bias PN junction is very close to one. As a result, the device conductance predominantly originates from the intrinsic conductance of the three segments comprising the CNT channel as well as the contacts resistance. Hence, we consider the three CNT-segments as three resistors in a row. In figure 3, G_1, G_2 and G_3 represent the conductance of the three channel parts. G_1 represents the middle segment of the CNT, which is placed above the local gate. G_2 and G_3 include the small (left and right) CNT-segments as well as the device contacts resistance (which are considered to be gate independent). The three conductances (G_1, G_2 and G_3) have different capacitances to the gate and are modulated according to the effective electric field applied by the gate electrode.

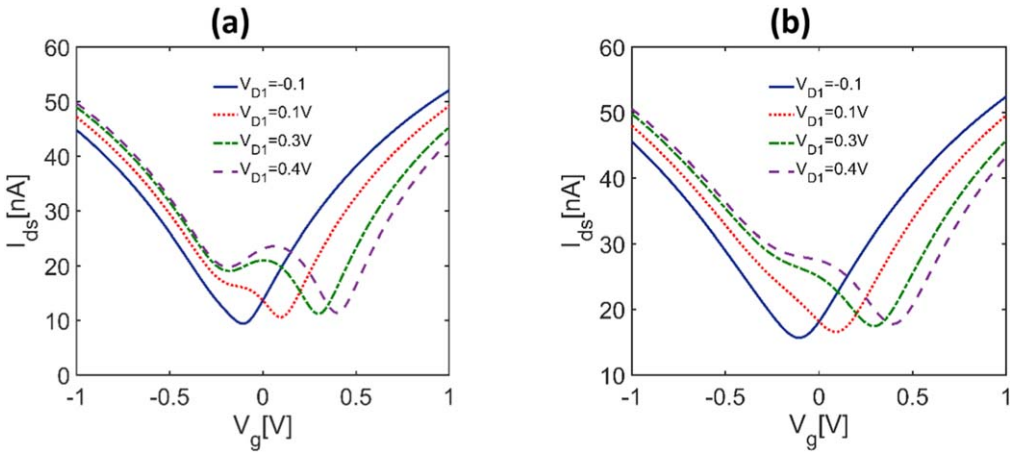

Figure 4. Simulation of the transfer characteristics development with V_{D1}. (a) The Dirac voltage of the CNT's middle segment (V_{D1}) changes as the LGD layer is charged or discharged. The simulation qualitatively reproduces the effect presented in figure 2(a). The intrinsic charges at the Dirac voltages of each segment along the CNT are taken to be, $n_{01} = 250\ \mu\text{m}^{-1}$, $n_{02} = n_{03} = 200\ \mu\text{m}^{-1}$. (b) The effect of extra intrinsic charge in the CNT, $n_{01} = 450\ \mu\text{m}^{-1}$, $n_{02} = n_{03} = 400\ \mu\text{m}^{-1}$. The double-Dirac points are less evident.

Electrical model

For the middle of the CNT-segment (G_1), we calculate the charge density according to:

$$N_1 = \sqrt{{n_{01}}^2 + \left(\frac{C_1(V_{gs} - V_{D1})}{q}\right)^2}, \quad (1)$$

where N_1 is the number of charges per 1 μm of the CNT-segment, q is the electron charge, n_{01} is the number of charges at $Vg = V_{D1}$ (intrinsic charge), V_{D1} is the Dirac voltage for the middle segment, and C_1 is the capacitance per 1 μm ($\text{F}\,\mu\text{m}^{-1}$) between segment 1 and the local gate. Therefore, the conductance of the middle segment is:

$$G_1 = \frac{q\mu N_1}{L_1}, \quad (2)$$

where μ is the electrical mobility.

For the left CNT-segment:

$$N_2 = \sqrt{{n_{02}}^2 + \left(\frac{C_2(V_{gs} - V_{D2})}{q}\right)^2}, \quad (3)$$

where N_2 is the number of charges per 1 μm of the left segment, n_{02} is the number of charges at $V_{gs} = V_{D2}$, and C_2 is the capacitance per 1 μm ($\text{F}\,\mu\text{m}^{-1}$). The conductance of this channel segment includes the contact resistance, therefore, the conductance G_2 is:

$$G_2 = \frac{1}{R_2} = \left(R_{LC} + \frac{L_2}{q\mu N_2}\right)^{-1}, \quad (4)$$

where R_{LC} is the left contact resistance. The calculations for the right segment conductance are similar to the left segment calculations, except that we may use the appropriate N_3, L_3, and R_{RC} (the right contact resistance). Finally, the total conductance of our device (G_{TOT}) is given by:

$$G_{TOT} = \left(\frac{1}{G_1} + \frac{1}{G_2} + \frac{1}{G_3}\right)^{-1}, \quad (5)$$

and the drain-source current is $I_{ds} = G_{TOT} \cdot V_{ds}$.

We utilize this model and explore the influence of the different parameters on the device conductance. Figure 4(a) demonstrates that our model can qualitatively predict the transfer characteristics depicted in figure 2(a). The double-Dirac-points (DDP) feature appears as V_{D1} grows, for a constant $V_{D2} = -0.2$ V. Figure 4(b) presents the effect of larger initial doping (n_{01} and n_{02}) on the transfer characteristics. Our simulations reveal that the DDP feature is more pronounced when n_{01} and n_{02} are small. In the simulation of figure 4(a), n_{01} and n_{02} are smaller by $200\ \mu\text{m}^{-1}$ charge density compared to their values in the simulation of figure 4(b). This can explain other devices, which presented less noticeable features than the one in figure 2(a).

To better observe the effect of charging of LGD on the DDP evolution, we use voltage pulse-trains with various amplitudes on the local gate, followed by an I_{ds} versus V_{gg} measurement, with a limited sweep-range (up to ± 0.7 V). The limited V_{gg} sweep-range allows us to observe both Dirac points without causing excess charging or discharging of the LGD. The pulse-train is composed of 6 $\times$ 1msec V_{lg} pulses, with duty cycle = 0.2, and $V_{lg} = 0$ V at the pulse's interval. Figure 5(a) depicts the transfer characteristics, measured directly after pulse-train sessions with V_{lg} amplitudes of 1.8, 2.1, 2.4, 2.7 and 3 V (colored dotted lines). We fit the data with the described model, assuming equivalence of the two side segments (gray circles), from which we can extract the physical parameters of our devices. Figure 5(b) presents the evolution of V_D for both types of CNT-segments. The Dirac voltage of the middle segment (V_{D1}) shows a clear p-doping increase as the pulse-train amplitude grows. On the contrary, the Dirac voltage of the left segment (V_{D2} of L_2 in figure 1(a)), is hardly affected. The additional doping of the L_1 CNT-segment as a function of V_{lg} pulse-train amplitude is presented in SI figure 2.

Additional fitting parameters include n_{01} and n_{02} which were found to be $\sim 260\ \mu\text{m}^{-1}$ and $\sim 200\ \mu\text{m}^{-1}$ respectively,

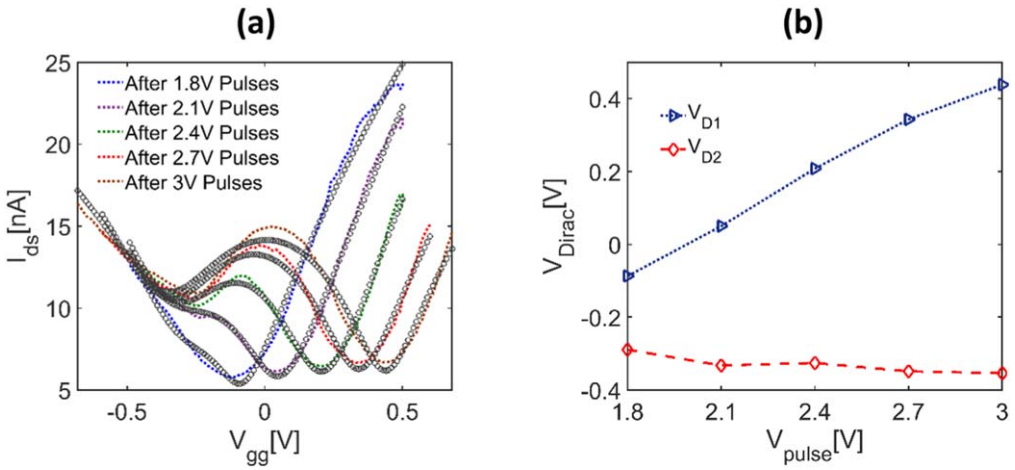

Figure 5. Transfer characteristics for $V_{ds} = 5$ mV after different V_{lg} pulse-trains. (a) Measurement (colored dotted lines) and simulation (gray circles) of I_{ds} versus V_{gg}. (b) Evolution of the Dirac points V_{D1} and V_{D2} of segments L_1 and L_2 (see figure 1(a)) respectively, according to the parameters extracted from the fitting in (a).

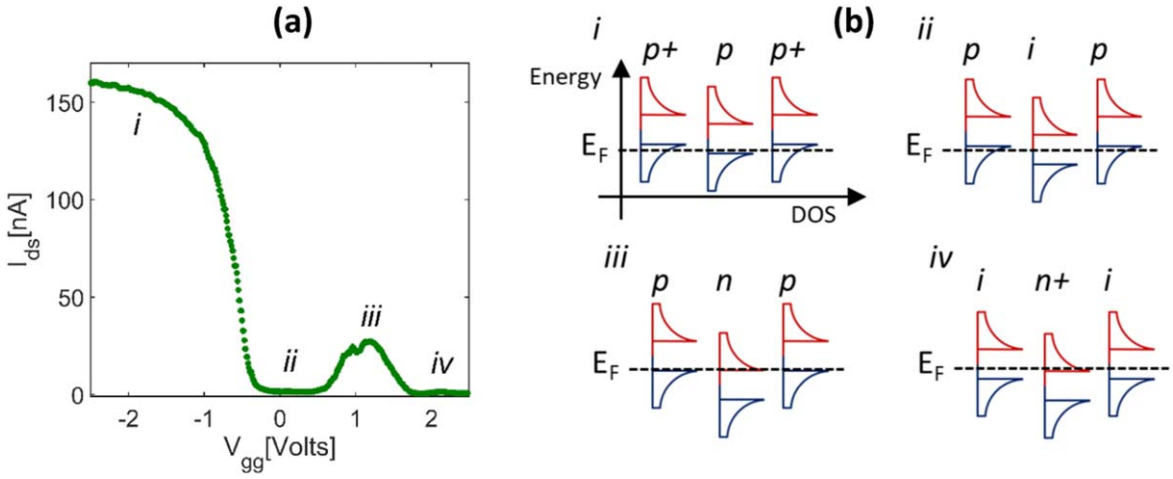

Figure 6. (a) Transfer characteristics of a SC-CNTFET for $V_{ds} = 40$ mV. The transfer characteristics is divided into four regions *i*–*iv*. (b) Fermi energy, and density of state (DOS) for the different segments along a small band-gap CNT, corresponding to the regions depicted in 'a'. The blue and red DOS are the CNT's valance and conduction bands respectively. In region *i* all CNT-segments are p-type, but the middle CNT-segment is 'slightly less p-type' due to positive charge in the gate-stack. In region *ii,* the middle segment is intrinsic (E_F in the middle of the band-gap), while both L_2 segments (see figure 1) are p-type. In region *iii,* the n-type middle segment, and p-type of both L_2 segments give rise to BTBT current. In region *iv*, higher V_{gg} voltages shift E_F of the L_2 segments into the band-gap, while the middle segment is strongly n-doped.

the electrical mobility $\mu \approx 1000\ \mathrm{cm^2\,V^{-1}{\cdot}sec^{-1}}$ and $R_c \approx 35\ \mathrm{k\Omega}$. The capacitances between the local or global gates and the CNT were calculated according to equation (6) and found to be $C_1 = 5 \times 10^{-16}\,\mathrm{F\,\mu m^{-1}}$ and $C_2 = 2 \times 10^{-16}\,\mathrm{F\,\mu m^{-1}}$ for the middle and the side segments of the CNT, respectively.

By incorporating a semiconducting carbon nanotube (SC-CNT) in the configuration presented in figure 1(a), we measure the transfer characteristics depicted in figure 6(a). The CNT is p-type, and as expected, for a negative $V_{gg} < V_{th}$ ($V_{th} \sim -0.25$ V), we observe a large rise in the drain current (I_{ds}). However, For $V_{gg} > V_{th}$ instead of zero current, we obtain a hump in the I_{ds} characteristics. We argue that the hump is a manifestation of an overlap between the DOS of holes, around the top of the valance band of the p-type CNT-segment, with the electrons DOS, around the bottom of the conductance band of the corresponding n-type CNT-segment [16, 22]. This overlap results in a BTBT current between the two CNT-segments. Unlike the device with metallic CNT, the hump is present in both V_{gg}-sweep directions. The absence of free states in the CNT's band-gap produces strong effective coupling between the V_{gg} and the CNT's electrochemical potential (due to low quantum capacitance). This coupling, which is much larger than for the m-CNT case, is the main reason for the differences in the respective behavioral-model. Moreover, the low DOS of the device at $V_{gg} > 1.5$ V inhibits the gate-stack charging for positive V_{gg}. Figure 6(b) proposes a simple model for the measured data, in which the

modulation of the charge along the CNT by the V_{gg} dominates over the electrostatic doping of the trap charges in gate dielectric.

For the estimation of the CNT's doping, we register the gate voltage at the middle of the I_{ds} hump, $V_M = 1.16$ V, and at both ends of the hump $V_L = 0.62$ V, $V_H = 1.7$ V. At V_M, there are two intramolecular PN junctions along the CNT, and the two sides of the junctions are degenerately doped with electrons or holes, for the middle or the right/left CNT-segments, respectively. For $0\,V < V_{gg} < V_L$, the middle segment is depleted from electrons, and for $V_H < Vgg < 2$ V, the right/left segments are depleted from holes. For a SC-CNT the total gate capacitance (C_T) must include both the quantum capacitance (C_q), and the geometrical capacitance (C_g). C_g is given by

$$C_g = \frac{2\pi \cdot \varepsilon_r \varepsilon_0}{a \cosh(2D/d)}, \tag{6}$$

where, $\varepsilon_0 = 8.85 \cdot 10^{-18} F\ \mu m^{-1}$, is the permittivity of the vacuum, D is the distance between the center of the CNT and the local gate, and d is the CNT diameter. Taking $D = 6$ nm, $d = 2.4$ nm and $\varepsilon_r = 16$ (HfO_2 relative dielectric constant) one finds $C_g = 3.88 \cdot 10^{-16}$ F um^{-1}. The quantum capacitance is computed based on John *et al* [23]:

$$C_q = \frac{q^2}{2k_B \mathrm{Th}} \sqrt{\frac{m^*}{2}} \int_0^\infty \frac{\nu(E)}{\sqrt{E}} \left[\mathrm{sech}^2\left(\frac{E + \frac{E_G}{2} - qV_a}{2k_B T} \right) + \mathrm{sech}^2\left(\frac{E + \frac{E_G}{2} + qV_a}{2k_B T} \right) \right] dE, \tag{7}$$

where m^* is the electron effective mass in the conduction band, $\nu(E)$is the number of energy bands between the middle of the band-gap (E_G) up to energy E, $qV_a = \mu$ is the CNT's electrochemical potential and h is Planck constant. We find $C_q - 1.4C_g$ at the middle of the 1st van Hove singularity (vHs) in the conduction band, and under assumption of symmetric picture for the holes in the valance band we calculate the effective gate capacitance:

$$C_T = \frac{C_q \cdot C_g}{C_q + C_g} \approx \frac{7C_g}{12} = 2.26 \cdot 10^{-16} \left[\frac{F}{\mu m} \right]. \tag{8}$$

At $V_g = V_M$ the charge carrier densities are approximately $n_e \sim n_h \sim C_T(V_M - V_L) \sim C_T(V_H - V_M) \approx 760$ e μm^{-1}. The estimated charge density is 2.5 electrons (or holes) per 1000 carbon atoms (see SI.A). We estimate the depletion-width at the middle of the I_{ds} hump ($V_m = 1.16$ V) according to two models and compare them. The first model adopts the textbook 3D PN junction calculation (full-depletion approximation), in which the 3D charge density is calculated from the the 1D charge density. The second model is based on the 1D depletion-width approximation proposed by Ilatikhameneh *et al* [24]. Considering that our CNT's band-gap is half the size used by Leonard and Tersoff [25], the 1D model nicely coincides with their derived depletion-width, and due to the high doping, both the 1D and 3D models estimate the depletion layer to be ~1.5 nm (see SI.B). We believe that this explains the efficient BTBT in our measured device.

Next, we wish to examine the PN junction behavior for E_F modulation along the different CNT-segments. For this purpose, we measure I_{ds} while sweeping the local gate, for several discrete V_{gg} values. Each V_{gg} value is kept fixed throughout the entire V_{lg} sweep cycle. These measurements are performed under vacuum ~10^{-4}Torr. We label three points along the transfer characteristics depicted in figure 7.

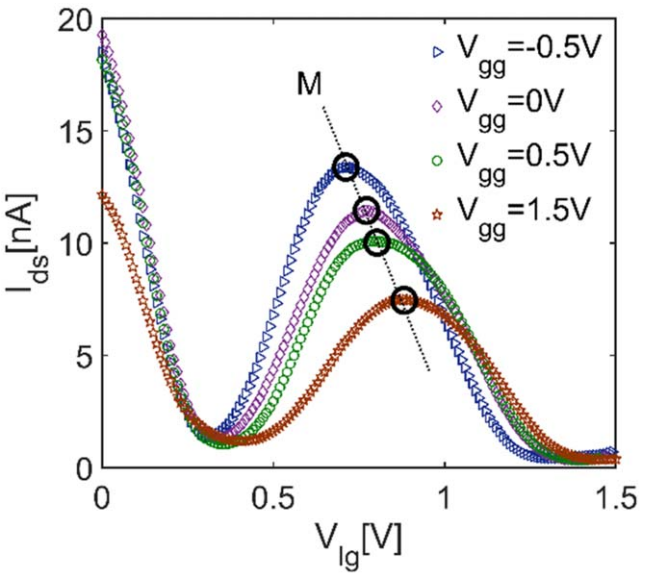

Figure 7. I_{ds} 'hump' arises due to doping variation in segment L_2 (see figure 1(a)). As V_{gg} increases, the 'hump' peak (labeled M and marked with dark circles) shifts to higher voltages (V_m) at which lower current (I_m) is measured. On the other hand, the hump widths hardly change for the different V_{gg} values. $V_{ds} = 40$ mV for all measurements.

The peak of the hump is labeled by M (middle), and its side ends by L and H for their lower and higher V_{lg} values, respectively. For each I_{ds} curve, points L are determined at the local minima on the left of the I_{ds} hump and points H are located at the point where $I_{ds} = 0.45$ nA on the right side of the hump. Figure 8(a) presents the effect of different V_{gg} on the position (V_M) and the magnitude of the I_{ds} hump (I_M). There is a linear relation between both I_M and V_M to V_{gg}. Figure 8(b) depicts the location of V_H and V_L as a function of V_{gg}. We obtain a slight increase in both V_H and V_L for larger V_{gg}, however the 'hump' width remains practically the same for all V_{gg}.

As evident from figure 7, the point where the middle section of the tube turns off ($V_{lg} = 0.35$ V) is the same for all V_{gg} values. This result is expected since the main part of L_1 is screened by the local gate and therefore the global gate voltage cannot affect this segment. However, as V_{gg} increases, the two side segments (L_2) are pushed further into their band gaps and their total conductance decreases. There are two consequences for this effect. The first is the increase of V_M for larger V_{gg}, as evident from figure 8(a) (blue symbols). For higher V_{gg} values, the condition for BTBT requires movement of the middle segment more into the n-type regime to be aligned with the valence band of the two L_2 segments. The second consequence is the decrease in the total current at the maximum point I_M (see figure 8(a), red symbols). The current reduction may occur due to the increase of the depletion layer

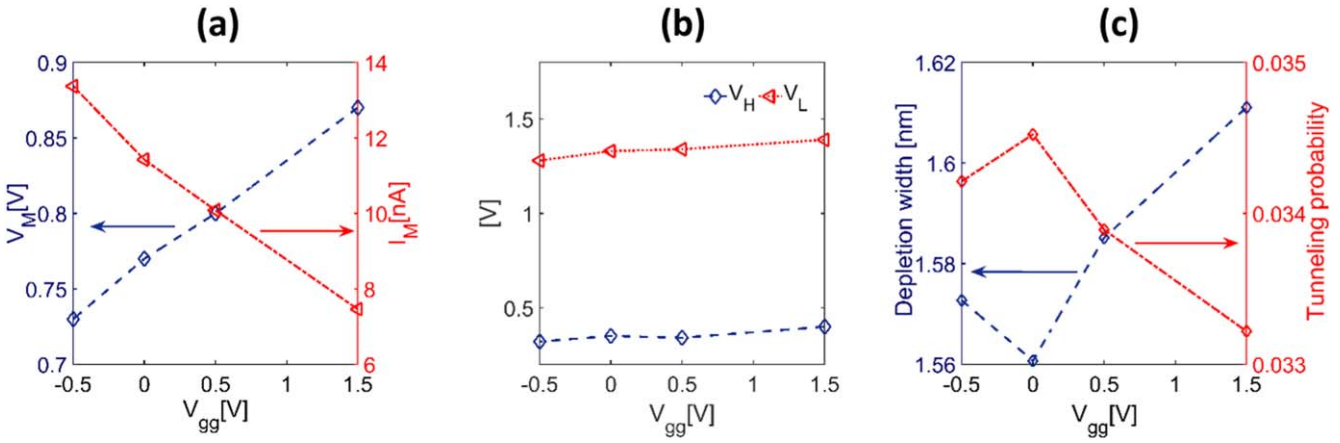

Figure 8. V_{gg} effect on the I_{ds} hump. (a) The hump peak position (V_M) and peak current (I_M) versus V_{gg} for the I_{ds} curves in figure 7. The different V_{gg} values are associated with doping variation in the CNT-segments close to the source and the drain. (b) The hump high (V_H) and low (V_L) local gate edge voltages versus V_{gg}. The hump position shifts slightly to a larger V_{lg} value as V_{gg} increases, while the hump width remains practically fixed at 0.99 V. (c) PN junction 1D depletion-width (see calculation in SI.B) and BTBT probability through the PN junction as calculated with equation (9).

of the PN junction for larger V_{gg}, or as a result of the lower conductance of the L_2 segments. To determine the cause, we calculated the transmission probability (T^{1D}) through the PN junction at V_M and found that the current reduction is mainly dictated by the L_2 segments. For the transmission probability calculation we used the Wentzel–Kramers–Brillouin (WKB) approximation T^{1D}_{WKB} [26, 27]. We assumed a triangular profile for the potential barrier with a width equals to the PN junction depletion-width, W_{1D}. The maximum barrier height equals E_G and the conductance band, E_c, of the n-type segment (L_1), coincides with the valence band, E_v, of the p-type side (L_2):

$$T^{1D}_{WKB} \approx \exp\left\{-W_{1D}\cdot\frac{4\cdot\sqrt{2m^*}E_G^{3/2}}{3\cdot\hbar\cdot(\Delta\Phi+E_G)}\right\}, \qquad (9)$$

where $\Delta\Phi$ is the energy window with DOS overlap for the n-type L_1 segment and p-type L_2 segment. We assume $\Delta\Phi = E_v^{L2} - E_c^{L1} \ll E_G$. W_{1D} is the depletion-width, which depends on the doping level of both sides of the PN junction (see SI.B). For the doping level we use the average doping of L_1 and L_2, ($n_e \sim C_T(V_M–V_L)/e$, $n_h \sim C_T(V_H–V_M)/e$) which is of the order of 10^{20}cm^{-3}. The tunneling probability presented in figure 8(c) is between 3.3 and $3.5\cdot10^{-2}$ for all V_{gg} values, and G_{Tun} is calculated as [28]:

$$\begin{aligned} G_{Tun} &= \frac{I_{Tun}}{V_{PN}} = \left(\frac{1}{V_{PN}}\right)\frac{4e^2}{h}T^{1D}_{WKB} \\ &\cdot\int_{Ec_{N-side}}^{Ev_{P-side}} f_{L1}(E) - f_{L2}(E)dE \approx \\ &\approx \left(\frac{1}{V_{PN}}\right)\frac{4e^2}{h}T^{1D}_{WKB} \\ &\cdot\frac{K_BT}{q}\ln\left[\frac{1}{2}\left(1+\cosh\left(\frac{V_{PN}}{K_BT/q}\right)\right)\right], \end{aligned} \qquad (10)$$

where V_{PN} is the potential drop across the PN junction. In the case of device conductance dominated by the tunneling conductance, $G \approx G_{Tun}$, the entire bias ($V_{ds} = 40$ mV) is expected to drop on the PN junction ($V_{PN} \approx V_{ds}$), and for $T^{1D}_{WKB} = 3.4\cdot10^{-2}$, $G_{Tun} \approx 5.4 \pm 0.1\cdot10^{-6}$ [S]. The device total conductance (G) at $V_{lg} = V_M$, $G = \frac{I_{ds}}{V_{ds}} \approx \frac{12nA}{40mV} = 3\cdot10^{-7}[S]$, is significantly lower than G_{Tun}. This result confirms that indeed I_{ds} at V_M is governed mainly by the electrical conductance of all three CNT-segments. However, as expected, for higher V_{gg} the depletion-width is larger, and the transmission probability is smaller as depicted in figure 8(c). The contribution from thermionic current through the PN junction is negligible, as evident from the current decrease for larger V_{lg} due to the increase of the depletion-width and the reduction of the BTBT.

The results presented here where measured at room temperature, and show no dependence on the CNTs diameter (2–3 nm) or length of L_1 segment length (2.8–3.8 μm) or L_2 length (0.6–0.3 μm). An interesting follow up of this work may include examination of the effect of temperature on BTBT through the intramolecular PN junction. The comparison may be tricky since at low temperature BTBT is expected to decrease (equation (10)), at the same time some of the effects presented in this work may disappear completely due to smaller doping of the LGD. Moreover, the intrinsic behavior of the CNT's segments will change as a result of the high vacuum and low temperature will cause quantum confinement effects in the various CNT-segments.

Summary

We present intramolecular PN junctions in both small band-gap and semiconducting carbon nanotubes. The effective LGD doping at the CNT's middle segment (L_1) forms by the global gate is a result of a thin LGD and the relative capacitance between C_3 and C_1 (figure 1(a)). A strong electrostatic leaver of the global gate requires $C_3 \gg C_1$ (in our geometry $C_3 \approx 10C_1$). The PN junctions in m-CNTs are formed and erased due to charging and discharging of charge traps in the local gate dielectric. We developed a conductance model for m-CNTs which agrees well with our measurements and affirms that the electrostatic doping occurs mainly in the middle segment of the CNT, which overlaps with the local gate. The proximity of the trap charges to the CNT

interface is responsible for the sharp and narrow PN junctions. The formation and destruction of these PN junctions along the CNT depend on the local gate voltage sweep-range and are highly reproducible (we measured over five different devices which show the PN junction signature). For SC-CNTs we observe a clear BTBT. Detailed analysis of the measurements based on the WKB approximation reveals a very narrow depletion region length of a few nm and high transmission probability of approximately $5 \cdot 10^{-2}$ at the optimal energy bands overlap. Unlike for m-CNTs the local doping remains unchanged regardless of the gate voltage polarity we apply. These results may assist in developing a non-volatile one-dimensional PN junction memory cell and in designing a tunneling based field effect transistor.

Acknowledgments

This study was supported by the MOST (Grant No. 3-14678), and the Russell Berrie Nanotechnology Institute. The work made use of the Micro Nano Fabrication Unit at the Technion. G Z acknowledges support by the Russel Berrie scholarships.

Data availability statement

All data that support the findings of this study are included within the article (and any supplementary files).

ORCID iDs

Yuval E Yaish https://orcid.org/0000-0001-7997-5457

References

[1] Venkataraman A, Amadi E V, Chen Y and Papadopoulos C 2019 Carbon nanotube assembly and integration for applications *Nanoscale Res. Lett.* **14**

[2] Todri-Sanial A, Magnani A, De Magistris M and Maffucci A 2016 Present and future prospects of carbon nanotube interconnects for energy efficient integrated circuits *2016 17th Int. Conf. Therm. Mech. Multi-Physics Simul. Exp. Microelectron. Microsystems, EuroSimE 2016* pp 1–5

[3] Itami K and Maekawa T 2020 Molecular Nanocarbon science: present and future *Nano Lett.* **20** 4718–20

[4] Anzar N, Hasan R, Tyagi M, Yadav N and Narang J 2020 Carbon nanotube—a review on synthesis, Properties and plethora of applications in the field of biomedical science *Sensors Int.* **1** 100003

[5] Cardenas J A, Andrews J B, Noyce S G and Franklin A D 2020 Carbon nanotube electronics for IoT sensors *Nano Future* **4** 12001

[6] Biercuk M J, Shahal Ilani C M M and McEuen P L 2008 Electrical transport in single-wall carbon nanotubes *Carbon Nanotubes* (*Top. Appl. Phys.*) ed A Jorio, G Dresselhaus and M S Dresselhaus 111 (Berlin, Heidelberg: Springer) 455–92

[7] Wildöer J W G, Venema L C, Rinzler A G, Smalley R E and Dekker C 1998 Electronic structure of atomically resolved carbon nanotubes *Nature* **391** 59–62

[8] Javey A, Guo J, Farmer D B, Wang Q, Wang D, Gordon R G, Lundstrom M and Dai H 2004 Carbon nanotube field-effect transistors with integrated ohmic contacts and high-κ gate dielectrics *Nano Lett.* **4** 447–50

[9] Kong J, Cao J, Dai H and Anderson E 2002 Chemical profiling of single nanotubes: intramolecular p-n-p junctions and on-tube single-electron transistors *Appl. Phys. Lett.* **80** 73–5

[10] Appenzeller J, Lin Y M, Knoch J and Avouris P 2004 Band-to-band tunneling in carbon nanotube field-effect transistors *Phys. Rev. Lett.* **93** 1–4

[11] Lee J U, Gipp P P and Heller C M 2004 Carbon nanotube p-n junction diodes *Appl. Phys. Lett.* **85** 145–7

[12] Liu X *et al* 2016 A p−i−n junction diode based on locally doped carbon nanotube network *Sci. Rep.* **6** 1–6

[13] Gabor N M, Zhong Z, Bosnick K, Park J and McEuen P L 2009 Extremely efficient multiple electron-hole pair generation in carbon nanotube photodiodes *Science* **325** 1367–71

[14] Liu C H, Wu C C and Zhong Z 2011 A fully tunable single-walled carbon nanotube diode *Nano Lett.* **11** 1782–5

[15] Feng X, Zhao X, Yang L, Li M, Qie F, Guo J, Zhang Y, Li T, Yuan W and Yan Y 2018 All carbon materials pn diode *Nat. Commun.* **9** 1–7

[16] Hatakeyama R, Li Y F and Kaneko T 2007 Transport properties of p-n junctions created in single-walled carbon nanotubes by Fe encapsulation *2007 7th IEEE Int. Conf. Nanotechnol.—IEEE-NANO 2007, Proc.* vol 1, pp 180–4 (http://hdl.handle.net/10097/46678)

[17] Chen C *et al* 2016 Carbon nanotube intramolecular p−i−n junction diodes with symmetric and asymmetric contacts *Sci. Rep.* **6** 1–7

[18] Xu J L, Dai R X, Xin Y, Sun Y L, Li X, Yu Y X, Xiang L, Xie D, Wang S D and Ren T L 2017 Efficient and reversible electron doping of semiconductor-enriched single-walled carbon Nanotubes by using decamethylcobaltocene *Sci. Rep.* **7** 1–10

[19] Esconjauregui S, AU-D'Arsié L, AU-Guo Y, AU-Yang J, AU-Sugime H, AU-Caneva S, AU-Cepek C and AU-Robertson J 2015 Efficient transfer doping of carbon Nanotube Forests by MoO_3 *ACS Nano* **9** 10422–30

[20] Amer M R, Chang S W and Cronin S B 2015 Competing photocurrent mechanisms in quasi-metallic carbon Nanotube pn devices *Small* **11** 3119–23

[21] Knoch J, Mantl S and Appenzeller J 2007 Impact of the dimensionality on the performance of tunneling FETs: bulk versus one-dimensional devices *Solid. State. Electron.* **51** 572–8

[22] Zhou C, Kong J, Yenilmez E and Dai H 2000 Modulated chemical doping of individual carbon nanotubes *Science* **290** 1552–5

[23] John D L, Castro L C and Pulfrey D L 2004 Quantum capacitance in nanoscale device modeling *J. Appl. Phys.* **96** 5180–4

[24] Ilatikhameneh H, Ameen T, Chen F, Sahasrabudhe H, Klimeck G and Rahman R 2018 Dramatic impact of dimensionality on the electrostatics of PN junctions and Its Sensing and Switching Applications *IEEE Trans. Nanotechnol.* **17** 293–8

[25] Léonard F and Tersoff J 1999 Novel length scales in nanotube devices *Phys. Rev. Lett.* **83** 5174–7

[26] Sze S M and Kwok K N 2007 *Physics of semiconductor devices* 8 3rd (Hoboken, NJ: Wiley-Interscience) 417–28

[27] Ilatikhameneh H, Salazar R B, Klimeck G, Rahman R and Appenzeller J 2016 From Fowler-Nordheim to Nonequilibrium Green's function modeling of tunneling *IEEE Trans. Electron Devices* **63** 2871–8

[28] Jena D, Fang T, Zhang Q and Xing H 2008 Zener tunneling in semiconducting nanotube and graphene nanoribbon p-n junctions *Appl. Phys. Lett.* **93**